Atomic force microscopy and in situ-annealing X-ray diffraction study on template-stripped gold substrates for optimum self-assembled monolayer deposition

E. Sanchez-Adaime, D. Duché, S. Escoubas, V. Jangid, L. Nony, A. Moreau, J. Lumeau, L. Patrone, C. Lebouin, L. Escoubas

▶ **To cite this version:**

E. Sanchez-Adaime, D. Duché, S. Escoubas, V. Jangid, L. Nony, et al.. Atomic force microscopy and in situ-annealing X-ray diffraction study on template-stripped gold substrates for optimum self-assembled monolayer deposition. Thin Solid Films, 2021, 739, pp.138978. 10.1016/j.tsf.2021.138978 . hal-03436579

HAL Id: hal-03436579
https://amu.hal.science/hal-03436579v1

Submitted on 20 Nov 2021

HAL is a multi-disciplinary open access archive for the deposit and dissemination of scientific research documents, whether they are published or not. The documents may come from teaching and research institutions in France or abroad, or from public or private research centers.

L'archive ouverte pluridisciplinaire **HAL**, est destinée au dépôt et à la diffusion de documents scientifiques de niveau recherche, publiés ou non, émanant des établissements d'enseignement et de recherche français ou étrangers, des laboratoires publics ou privés.

Distributed under a Creative Commons Attribution - NonCommercial - NoDerivatives 4.0 International License

Atomic force microscopy and in situ-annealing X-ray diffraction study on template-stripped gold substrates for optimum self-assembled monolayer deposition

E. Sanchez-Adaime[a], D. Duché[a*], S. Escoubas[a], V. Jangid[a,b], L. Nony[a], A. Moreau[c], J. Lumeau[c], L. Patrone[d], C. Lebouin[b] and L. Escoubas[a]

[a]Aix Marseille Univ, CNRS, Université de Toulon, IM2NP, UMR 7334, F-13397 Marseille, France

[b]Aix Marseille Univ, CNRS, MADIREL, UMR 7246, F-13397 Marseille, France

[c]Aix Marseille Univ, CNRS, Centrale Marseille, Institut Fresnel, 13013 Marseille, France

[d]Aix Marseille Univ, CNRS, Université de Toulon, IM2NP UMR 7334, Yncréa Méditerranée, ISEN Toulon, Maison du Numérique et de l'Innovation, Place G. Pompidou, F-83000 Toulon, France

IM2NP address:
IM2NP - Site de Polytech Marseille
Bâtiment Louis NEEL - Technopôle de Château Gombert
5 rue Enrico Fermi
F-13453 MARSEILLE Cedex 13 – France

*Corresponding author:
e-mail address : david.duche@im2np.fr
postal address:
Faculté des Sciences de Saint Jérôme - Case 142
Avenue Escadrille Normandie Niemen
F-13397 Marseille Cedex 20 – France

Abstract

Literature is well supplied with studies of gold deposit on mica for fabricating ultra-flat template-stripped gold surface. Gold on silicon has not received much attention. Our study optimizes the deposition rates, annealing temperatures and time to obtain a template-stripped gold surface with a very low roughness and large (111) oriented crystallites. Atomic force microscopy is performed in tapping and peak force mode to evaluate the surface roughness. The crystallite size is obtained from in situ X-ray diffraction measurements during

annealing. We find out that a deposition rate of 0.2 nm/s with a 40 min annealing at 400°C gives the best result (0.21±0.04) nm.

Key-words: Ultra-flat substrates; Atomic force microscopy; X-ray diffraction; Self-assembled monolayer; Template-stripped gold; Crystallite size

1. Introduction

With the development of studies on nanometric or micrometric objects and plasmonic, the requirements on specific substrates have increased. The physical and chemical properties are optimized to achieve the most suitable substrate for the study. In the case of metallic surfaces, such as gold, these optimizations have been achieved by studying the deposition parameters[1–9], the nature of the substrate [10–14], annealing [4,9,11–18] and other surface treatments [5,11,13,15–17,19,20]. One of the objectives is to increase the flatness of the surface. Template-stripping, which consists of depositing metal on flat substrate and exposing the metal surface at the interface with the substrate, has revealed to be an easy access to ultra-flat surfaces [12,13,15,16].

Gold is a non-toxic noble metal which is stable in ambient conditions and an excellent candidate for grafting molecules using anchoring groups such as thiol and thiolacetate [21–23]. The latter point, with the chemical stability, make gold suitable for self-assembled monolayer (SAM) studies [24–28]. However, the mechanical and electrical properties of the SAM are influenced by its organization [26,29–32]. Supplying a low roughness surface, such as ultra-flat surfaces obtained from template-stripping, is one of the main possibilities to guarantee a well-organized SAM.

Template-stripped gold (AuTS) samples was prepared by Hegner [15] and Wagner [16]. They deposited gold on mica substrates and they observed the effect of annealing during deposition on roughness. They also compared the roughness of the as-deposited gold and the AuTS. The temperature range was from 20-25 °C to 600 °C. The lowest root mean square (rms) roughness they obtained by Atomic Force Microscopy (AFM) measurements was 0.28 nm (Temperature=20-25 °C). Moreover, the as-deposited gold roughness was one order of magnitude greater than AuTS. Once annealed, they tried different glues (epoxy glues and ceramic glues) for the stripping stage. Regardless of glue type, the AuTS roughness remains approximately the same. Stamou *et al.* [33] have adapted the techniques by using silicon wafers as substrates. They obtained a rms roughness of 0.4-0.5 nm.

Diebel *et al.* [12] investigated the effect of the nature of the substrate on the AuTS roughness at 35 °C and 300 °C during deposition. The studied substrates were mica, float glass and polymer-coated silicon. They did not use glue for making their AuTS, instead, they deposited a thick nickel layer (~200 µm) by electroplating. The mica substrate has given the lowest rms roughness of 0.3 nm at 300 °C.

Weiss *et al.* [13] proposed different methods for obtaining AuTS. They used optical adhesives (stable in ethanol compared to epoxy glues) and soldering to make the support for stripping. They obtained flexible AuTS with silicon as the template substrate. It was annealed in ambient air at 710 °C after deposition. AuTS obtained with optical adhesive and glass support give ~0.5 nm of rms roughness. Their result was higher than Diebel's or Hegner and Wagner's roughness, but they used silicon instead of mica substrates and the gold layer was annealed in ambient conditions after deposition and not inside a vacuum chamber during deposition.

Banner *et al.* [18] and Borukhin and Pokroy [19] works addressed the defects induced by template-stripping. In both cases, AuTS is studied and the template substrate is in silicon. In the first one, the pinhole defects are suppressed by a flame annealing of the gold surface prior template-stripping. The flame annealing is performed with a laboratory Bunsen burner fed with natural gas. By adjusting the distance between the gold surface and the flame, they reduced the number of defects. Borukhin *et al.* show the presence of twinning and stacking faults and propose methods for getting rid of them such as performing the stripping phase in ethanol or spectrophotometric-grade isopropyl alcohol. Nirmalraj *et al.* [11] made a similar study of removing gold layer defects on (111) oriented gold on mica and CaF_2 substrates. However, none of the studies mentioned above have addressed the deposition rate and the annealing (temperature and time) after deposition of the gold on silicon.

Our study precisely addresses these parameters on gold deposited on silicon wafer. We aim at optimizing the deposition rate and the annealing temperature and time in ambient conditions. The purposes of these optimizations are to obtain an ultra-flat gold surface with maximum and large (111) oriented crystallites. We are focused on the (111) orientation as thiol compounds, like alkanethiols, have their best compactness and small tilt angle on (111) orientation when deposited on gold [34,35]. Even if the literature is rich on smoothing AuTS on mica, there is no such studies on silicon. Silicon has one major advantage on mica with template-stripping that is there is no risk of chemical contamination of gold by silicon during stripping [15,33]. To achieve the current study purposes, in situ X-ray diffraction (XRD) during annealing and AFM in tapping and peak force modes are performed. Contrary to other studies[9,11,18,19,36,37], XRD measurements are performed during isotherms in order to have a better insight on the evolution of gold planes and crystallites with annealing.

In the following sections, the sample fabrication is firstly described with the methodology applied during this study (cf. section 2 and 3 respectively). Once samples are described with the analysis and the details on the used materials and equipment, the results of these analyses are developed in section 4, starting with AFM for selecting the right deposition rate, then the XRD for finding potential optimal temperature-annealing time couples, and finishing with AFM for selecting the optimal couple. The section 5 discusses the foregoing results in the same order. Finally, the main article conclusions are reminded.

2. Sample Fabrication

The template-stripped gold samples are made by following the procedure described below (cf. Fig. 1).

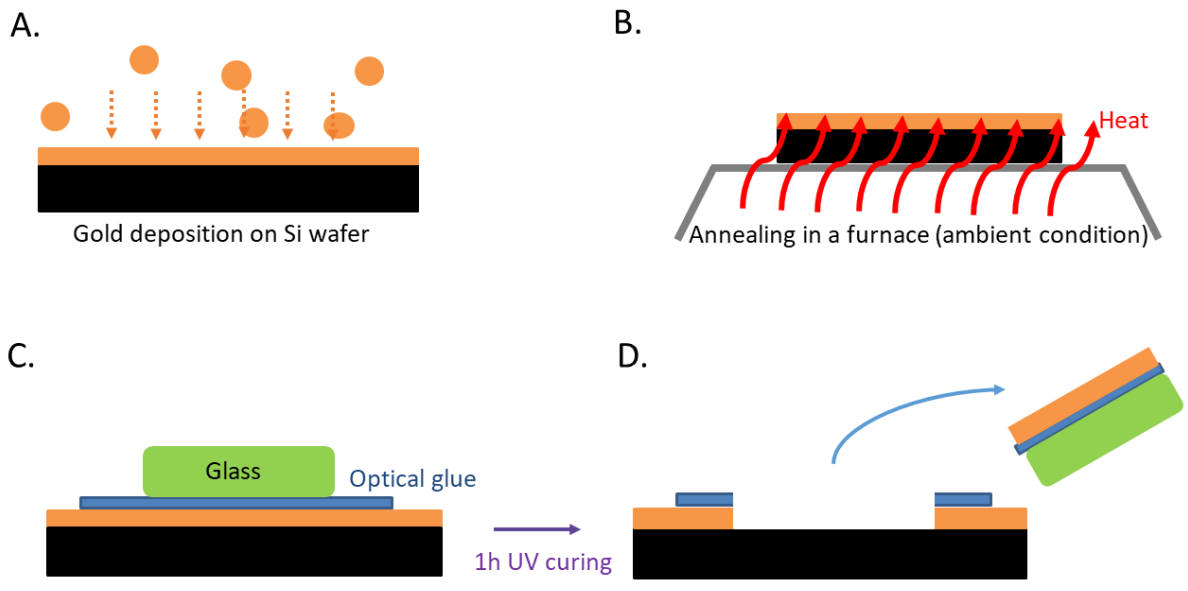

Fig. 1: Schematic of the different steps to fabricate template-stripped gold substrate (AuTS)

2.1. Evaporation step

A clean (100) orientated silicon wafer is introduced in the box coater chamber. The silicon wafers are ordered from Silicon Materials. They are P-doped, (100) oriented and (525±25) µm thick with one face polished and the other etched. The silicon wafers are unpacked in the clean room in which the box coater is. They are inserted in the box coater as received from Silicon Materials who cleaned them before sending them to us. Gold is deposited on the polished face. The box coater chamber used is an electron beam deposition boxcoater SYRUSpro 710 from Bühler. Once the pressure is stabilized at $5x10^{-2}$ Pa, the electron beam is started. The gold deposition is made at a constant rate to reach a final thickness of 200 nm. The gold pellets have the reference number P0489187 from Umicore. They are 99.99 % pure and measure 2-3 mm of diameter. To ensure a constant rate which is crucial for thin layers, the gold pellets are completely melted before deposition on the silicon wafer. Moreover, the deposition rate is measured thanks to a quartz microbalance and controlled with the current intensity used to evaporate gold. The modifications of the current to ensure a constant deposition rate depend on the amount of gold in the crucible, the chamber pressure, and the electron beam parameters.

When the gold atoms reach the silicon surface, they diffuse on it and they can desorb easily as the bonds with silicon are weak. In parallel of the desorption, two or more atoms can join together during their diffusion and form a nucleus that grows into hemispherical grain by collecting other diffused atoms. These grains appear aleatory on the silicon surface and their size increases more laterally than vertically. Once grains touch one another, they can merge into one larger grain at the expense of their mobility on silicon. As soon as all the silicon surface is covered with gold grains, the lateral growth stop and all supplementary Au atoms participate at the vertical increase. [38,39]

Therefore, the deposition rate could influence the nucleation, expansion and coalescence processes of the gold grains and, potentially, modify the final roughness of the surface. For this study, gold is deposited at 0.05 nm/s, 0.2 nm/s or 5 nm/s (cf. Fig. 1A) in order to determine the speed giving the less rough surface. During the deposition, the pressure can reach $5x10^{-1}$ Pa while gold is evaporating due to partial vapor pressure. The silicon substrate remains at room temperature (21 °C), contrary to previous studies in literature [11,12,15,16] where the deposition is made at high temperature (25 °C to 600 °C [15], 300 °C [16], 35 °C to 400 °C [12] and 300 °C to 650 °C [11]) on mica.

2.2. Annealing step

Once gold is evaporated on the (100) silicon wafer, annealing is performed which is not only crucial for the crystallite size but also for the surface roughness. The heat of annealing gives enough energy to gold atoms so that they can diffuse on the silicon substrate. Therefore, there is a reorganization of gold atoms resulting in the movement of crystallite boundaries which can enlarge the crystallite size and reduce the roughness. The annealing is made in a furnace under ambient air (cf Fig. 1B) and not inside the vacuum chamber of an evaporator[11,12,15,16] or on a flame [18] in ambient air. The silicon wafer covered by the gold film is directly placed in a furnace and then is brought from room temperature to the target temperature during a precise time. The chosen temperature and annealing time ranges for this study are given in the section 3.

The maximal temperature examined in this study is 500°C whereas gold and silicon form an eutectic at (363±2) °C [40]. If the Au-Si eutectic appear, the gold atoms will quickly diffuse in the silicon destroying the smooth interface between gold and silicon and preventing the ability to strip the gold from the substrate [19]. In our case, even at 500 °C, we could strip

the AuTS sample without any difficulties thanks to the native silicon oxide layer of our wafers. Indeed, the silicon oxide layer on Si wafers have demonstrated to be able to hinder the creation of the Au-Si eutectic [19].

2.3. Stripping step

Glass pieces of approximately 1cmx1cm are cut from a glass microscope slide using a diamond tip. These microscope slides are from VWR with the reference number ECN 631-1550. These glass pieces are ultrasonicated successively in a bath of deionized water, ethanol and propan-2-ol. Then, the non-damaged face of the glass pieces is exposed to an oxygen plasma for 2 minutes. Indeed, during cutting process, one of the glass face can be scratched. To minimize risks, we prefer not to use this face during gluing process.

Just after the annealing step, these clean glass pieces are stuck on the gold surface with an optical glue (cf. Fig. 1C). The optical glue used is Norland Optical Adhesive 61. The optical glue is cured inside a UV-KUB 2 with a full and continuous illumination at maximum power of 180W during 1 h. The plasma-exposed face is in contact with the glue. The glue is cured by exposing the wafer to UV-Lamp during 1 h.

Once cured, a cutter or a scalpel is used to cut the thin gold and cured glue layers around a glass piece. Then, with tweezers, the glass piece and the gold beneath it are stripped from the silicon wafer (cf. Fig. 1D). The gold surface that was facing silicon is now on the top of the template-stripped gold substrate [15] (AuTS). This surface is rinsed with ethanol and dried under a nitrogen stream.

3. Followed methodology

3.1. Selection of the deposition rate

In order to identify the optimized deposition rate, gold is deposited at different deposition rates (0.05 nm/s, 0.2 nm/s and 5 nm/s). All the samples have been annealed at 200 °C during 20 min. For simplicity, the name of the samples is abbreviated like AuTS0.5As which represents the nature (gold template-stripping) and the deposition rate (0.05 nm/s) of the metallic sample. The rms roughness and the useful surface, parameter that we define as the surface portion with low rms roughness, are checked by AFM measurements (cf. subsection 3.3). The deposition rate that leads to the lowest rms roughness with the largest useful surface will be chosen to perform the annealing study.

3.2. In-situ-annealing XRD protocol

XRD is used in θ/2θ mode to monitor the crystallite size, orientation evolutions and the inter-planar distance during annealing of the gold surface depicted in step B of Fig. 1. XRD diffractometer is a PANalytical Xpert pro MRD. The sealed X-ray source is copper made and is coupled with a parabolic mirror and a monochromator. The parabolic mirror parallelizes the Cu radiations. The monochromator is made of two parallel Ge(220) crystals and allows the selection of the copper Kα1 radiation (8.05 keV). Samples are mounted on a vertical goniometer which allows to rotate the samples around the 3 axes of rotation θ, φ and ψ. The X-ray sensor is a proportional PW1711 detector with a parallel slit collimator.

The crystallite size l is calculated with the Scherrer equation [9,41] (eq. 3-1) and the inter-planar distance d_{hkl} using Bragg's law (eq. 3-2).

$$l = \frac{0.9\lambda}{\beta\, cos(\theta)} \qquad \text{eq. 3-1}$$

With l the crystallite size in nm, λ the X-Ray wavelength in nm, β the full width at half maximum, in radian of the XRD peak and θ the measured angular position of this peak.

$$2d_{hkl}\sin(\theta) = n\lambda \quad \text{eq. 3-2}$$

With d_{hkl} the inter-planar distance between the (hkl) planes in nm, θ the measured angular position of the Bragg peak, n (an integer) the diffraction order and λ the X-Ray wavelength in nm. For our applications, we focus on the first order (n=1) to monitor the distance evolution between the consecutive parallel planes. This part of the study is carried out in two steps.

The first step consists in determining a temperature interval containing the optimal temperature. We refer as “optimal temperature” for XRD measurements, the temperature for which the crystallites are the largest and with most of them (111) oriented. The furnace is a DHS1100 from Anton Paar, installed on the XRD goniometer. Temperature is measured with a Pt-Pt10Rh thermocouple. The temperature control is performed by the unit control TCU 200. During this step, the sample temperature is risen from room temperature up to 500°C at a speed of 60 °C/min. The XRD measurements are performed at 23 °C, then at 100°C and with 100 °C step to reach 500 °C. A last measure is taken at 30 °C, when samples have been cooled back. The measure time last for 10 min and the temperature is maintained constant during this time. The 2θ angle has a variation interval centered on each gold orientation of interest (cf. subsection 4.2).

In the second step, 2 temperatures are selected amongst the temperature interval determined in the preceding step. For each temperature, a gold sample, deposited at speed selected in the part 5.1, is maintained at this selected temperature. At the same time,

crystallite size and orientation evolutions are monitored during each isotherm. Therefore, the annealing temperature-time couple which maximizes the size of the crystallites and the number of oriented (111) crystallites can be determined at each temperature. The final choice to select the most optimized temperature-annealing time couple is done by considering the surface roughness on AuTS.

All the XRD measurements are performed on gold before template-stripping process as the optical glue cannot bear temperatures above 125 °C. Moreover, Bragg peaks on XRD curves are fitted with Gaussian or Lorentzian equations, using Origin 85 or a custom Python code made for this study. The Python code fits the mathematical function with the data by minimizing the Sum of Squared Residuals (SSR, cf. eq. 3-3), the function kept for analyzing a XRD peak at the different temperatures is the one which minimizes the most the SSR.

$$SSR = \sum_{i=1}^{n} (y_i - f(x_i))^2 \qquad \text{eq. 3-3}$$

With n the number of data point for which the i^{th} datum is the couple $(x_i;y_i)$ and f is the function to fit on the data.

3.3. AFM protocol

AFM analyses are performed either with a Multimode 8 from Bruker, equipped with a Nanoscope V controller and the software Nanoscope 9.1, or with a Nano-Observer from CSINSTRUMENTS with the use of the software Nanosolution. Analyses are made either in peak force mode (Multimode 8) or in tapping mode (Nano-Observer). Peak force mode is performed with Multi75Al-G tips from BudgetSensors which have a resonance frequency range of 60-90 kHz, a force constant range of 1-7 N/m and a tip radius guaranteed inferior to 10 nm. For analyses made in tapping mode, the AFM tips used are PPP-NCLR from

Nanosensors which have a resonance frequency range of 146-236 kHz, a force constant range of 21-98 N/m and a tip radius guaranteed inferior at 10 nm. Each AFM is inside a box with anechoic moss on an optic table stabilized by pressurized air in a room controlled in temperature. Before starting experiments, the tip is let stabilized thermally and dynamically in the AFM during 24 h, if the tip is installed for the first time in the AFM, or during 1 h, if the tip is already installed.

Both AFM modes have the advantages to put less constraints on the AFM tips than contact mode, increasing tip lifetime and then the rms roughness measurement robustness. The scans are made at 256 pixels/s (px/s) for peak force mode and at 512 px/s in tapping mode. For both techniques, the scan size is 1µmx1µm on the gold surface after stripping (cf. Fig. 1D). AFM images are analyzed with Gwyddion 2.51 [42].

As shown in Fig. 2c, gold surface is not a monocrystalline structure. There are several grains and holes in the surface. The roughness inside a grain is expected to be low as a grain is a monocrystal. The roughness is mainly increased by the boundaries between grains and the holes in the gold surface.

Gwyddion software statistical quantities tool is used to evaluate the roughness and the useful surface [43]. The surface roughness is evaluated by computing the rms roughness on 3 to 5 images made at different locations on the samples. Then, the rms roughness mean and standard deviation are computed.

We define the useful surface as the portion of the image for which the rms roughness is below 0.3 nm. The 0.3 nm represents a very low rms roughness compare to literature [11–13,18,19] guaranteeing a flatness of high quality. Even if the rms roughness of the surface is superior to this limit, the surface is not necessarily useless as the roughness is mainly due to

the grain boundaries and holes which represents a tiny portion of the sample surface. Therefore, we develop a method to mask these height variations and evaluate the rms roughness out of this mask. We extend this mask to keep only the parts of the surface with a rms roughness inferior or equal to 0.3 nm which represents the useful surface.

The first step of this method is localizing the position and intensity of the height variations. For this purpose, Gwyddion has several functions like thresholding or edge detector. The method choice relies on exclusion of all holes and most possible boundaries by masking them and must be reproducible and weakly sensitive to the operators. This later condition is the most important. The best method in this study is to combine an edge detector by step and a thresholding.

More precisely, on the post-processed AFM image, the algorithm of edge detector by step is applied. This algorithm computes, at each pixel of the image, the square root difference between the 2/3 and the 1/3 quantiles of the heights in a radius of 2.5 pixels. The results are visualized in a second image called presentation. The colors in the presentation are a qualitative information of how prominent the edges are, or, in other words, how intense are the height variations (cf. Fig. 2a). The most prominent they are for the algorithm, the lighter they appear in the presentation. Then a height threshold is applied on the presentation. Doing so, the most prominent edges that correspond to holes and deep boundaries are masked (cf. Fig. 2b). The mask is extracted from the presentation and applied to the AFM image (Fig. 2c). If the rms roughness of the non-masked surface is higher or lower than 0.3 nm, the threshold is decreased or increased to have a non-masked surface with a rms roughness of 0.3 nm.

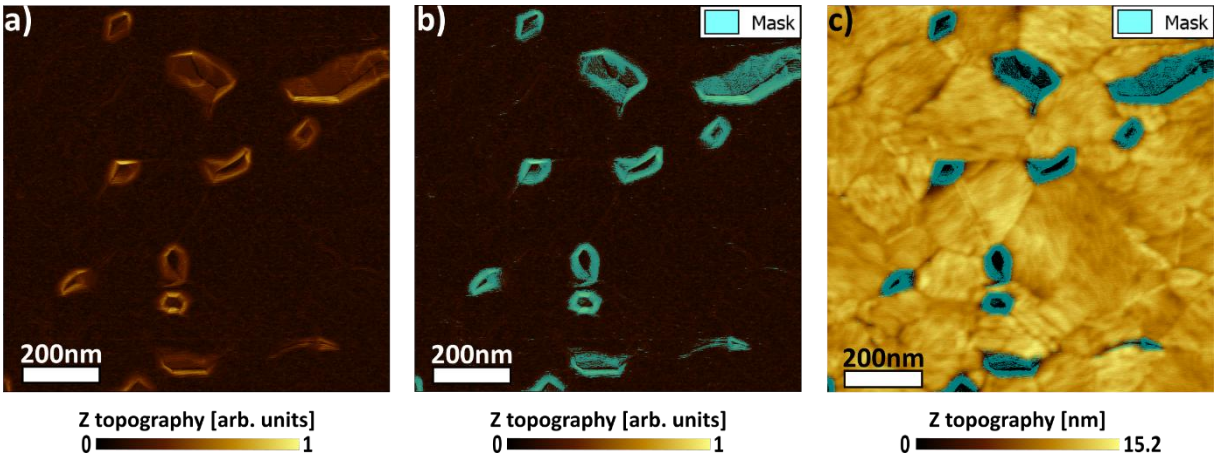

Fig. 2: Steps for determining the useful surface. a) Presentation obtained from the algorithm of edge detector by step on the AFM image. b) Masking the strong height variations using the thresholding tool. c) Applying the presentation mask on the AFM image. The image size is 1µmx1µm.

With the statistical quantities tool, the surface area is computed by following the profile of the grains. This area considers the height variations inside the grains.

3.4. Checking the surface suitability for SAM deposition

The verification of the suitability of our AuTS for SAM deposition is achieved by scanning tunneling microscopy (STM) and cyclic voltammetry (CV).

STM images are acquired with a Multimode 8 Nanoscope V from Bruker at ambient conditions in air on AuTS. The bias is applied to the sample relatively to the grounded mechanically sharpened Pt-Ir (95/5) wire used as STM tip. Different tips and samples are used to ensure reproducible and free from artifacts images. The tip-sample distance is controlled by tunneling current and voltage values of 10 pA and 200 mV respectively, and the scan rate is 512 px/s.

Moreover, CV is performed to verify how molecules organize on our AuTS. The CV measurements are carried out in a custom-built electrochemical cell equipped with a platinum counter electrode, an Ag/AgCl reference electrode and AuTS served as the working electrode. Potential is applied between the AuTS substrate and reference electrode and

corresponding response in terms of current is recorded between the AuTS substrate and Pt wire. The area of the substrate exposed to the electrolyte solution, equal to 0.5 cm^2, is controlled by using O-ring of 8 mm diameter. The cyclic voltammograms are measured in an aqueous solution of $HClO_4$ with a concentration of 1.0 M. We used the AUTOLAB PGSTAT302N with NOVA 2.10 software to record the cyclic voltammograms.

The molecules, characterized during CV measurements, are the 11-(Ferrocenyl) undecanethiol ($FcC_{11}SH$). The FcC11SH is purchased from Sigma-Aldrich and used without any further treatment.

4. Results

4.1. Deposition rates

Three deposition rates on gold have been studied: 0.05 nm/s, 0.2 nm/s and 5 nm/s. All the sample in this part have been annealed at 200 °C for 20 min.

At 0.05 nm/s (cf. Fig. 3), the mean rms roughness is (1.0±0.7) nm on all the surface which is too rough for SAM deposition. However, the mean useful surface is (95±3) %. So, 95.4 % of gold surface deposited at 0.05 nm/s have a sufficiently low roughness for molecules deposition. The remaining 4.6 % are the hole edges which have so intense height variations that they make the roughness jump from 0.3 nm to 1.0 nm.

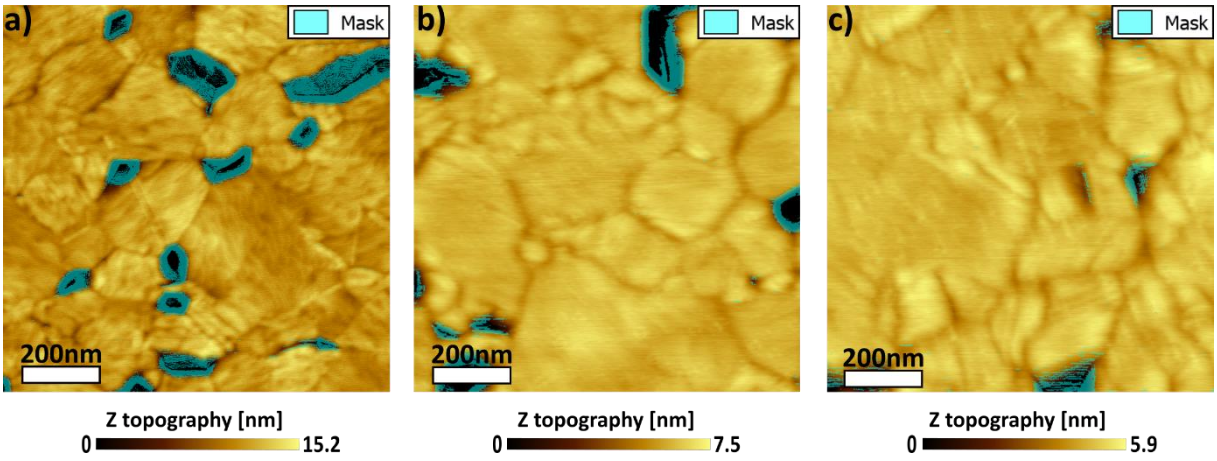

Fig. 3: AFM images on AuTS0.5As samples after annealing. a) to c) topographic images with applied mask so that the non-masked surface has a rms roughness inferior or equal to 0.3 nm.

When the speed is increased to 0.2 nm/s (Fig. 4), the mean rms roughness decreases to (0.26±0.03) nm with less dispersion across the surface. As the rms roughness is already below 0.3 nm, the useful surface is 100 %.

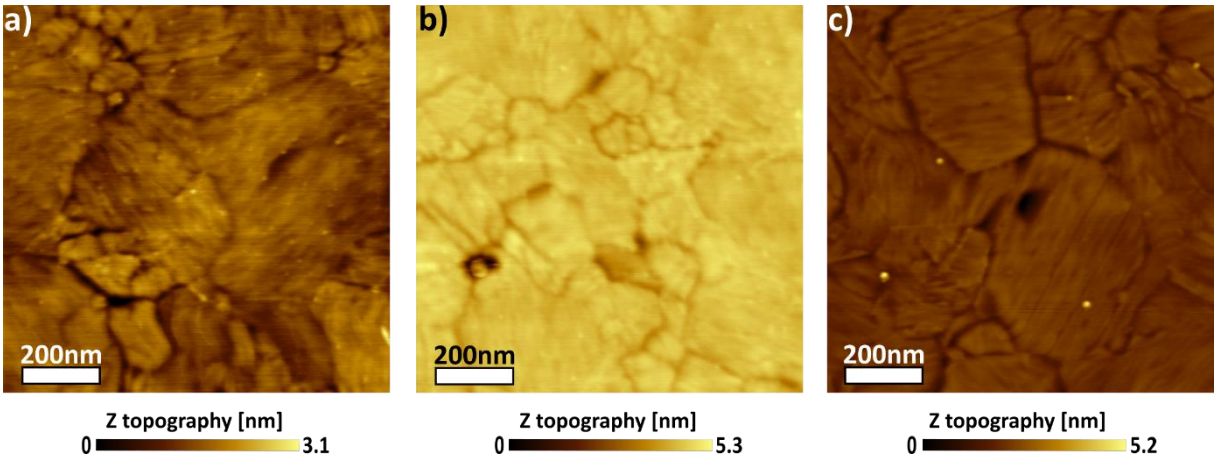

Fig. 4: AFM images on AuTS2As samples after annealing. a) to c) topographic images.

The substrate with the last deposition rate of 5 nm/s has (cf. Fig. 5) a mean RMS roughness of (0.9±0.2) nm and a mean useful surface of (79±18) %. So, even if the surface is rougher than the 0.3 nm limit, more than the four-fifth of the surface is below this limit, that is, the four-fifth of the surface is exploitable for deposition of molecules.

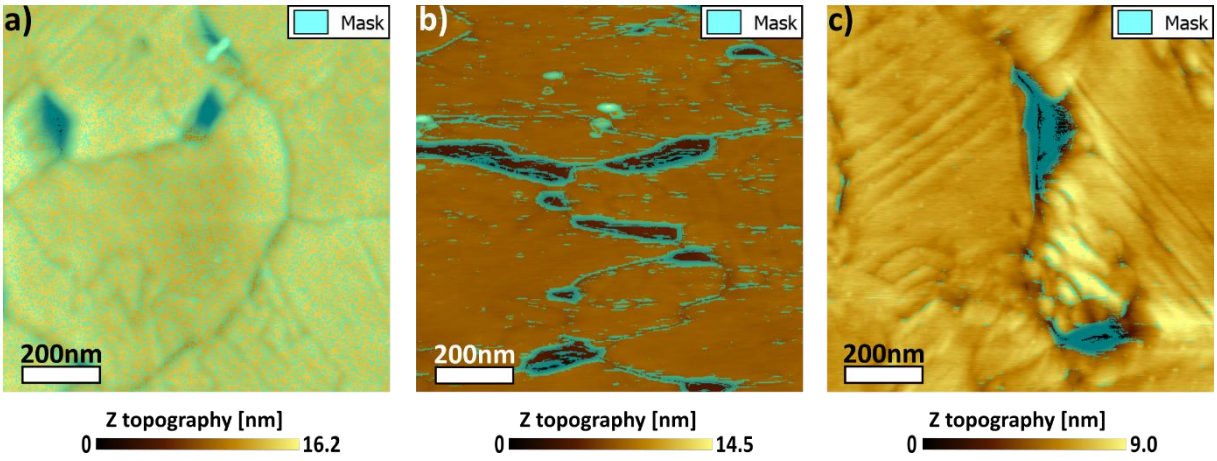

Fig. 5: AFM images on AuTS50As samples after annealing. a) to c) Images after mask application so that the non-masked surface has a rms roughness inferior or equal to 0.3 nm. For image a), the total pixel number of the image is 262,144 (512x512 px) and the mask occupies 110,100 px.

4.2. XRD measurements during temperature ramps

With a low roughness, a maximum of large (111) oriented gold crystallites is wanted for our AuTS surface. For this purpose, the different gold grain orientations must be determined. Indeed, the most prominent peak on XRD curves are selected in order to reduce the annealing time between the first and last measure at the same temperature. All XRD measurement are performed before stripping step on gold (cf. Fig. 1B).

We cleaved a part of the silicon wafer on which gold layer has been deposited at 0.2 nm/s and annealed at 200 °C before XRD measurement. We performed θ/2θ symmetric measurement on this sample and the result is displayed in Fig. 6a).

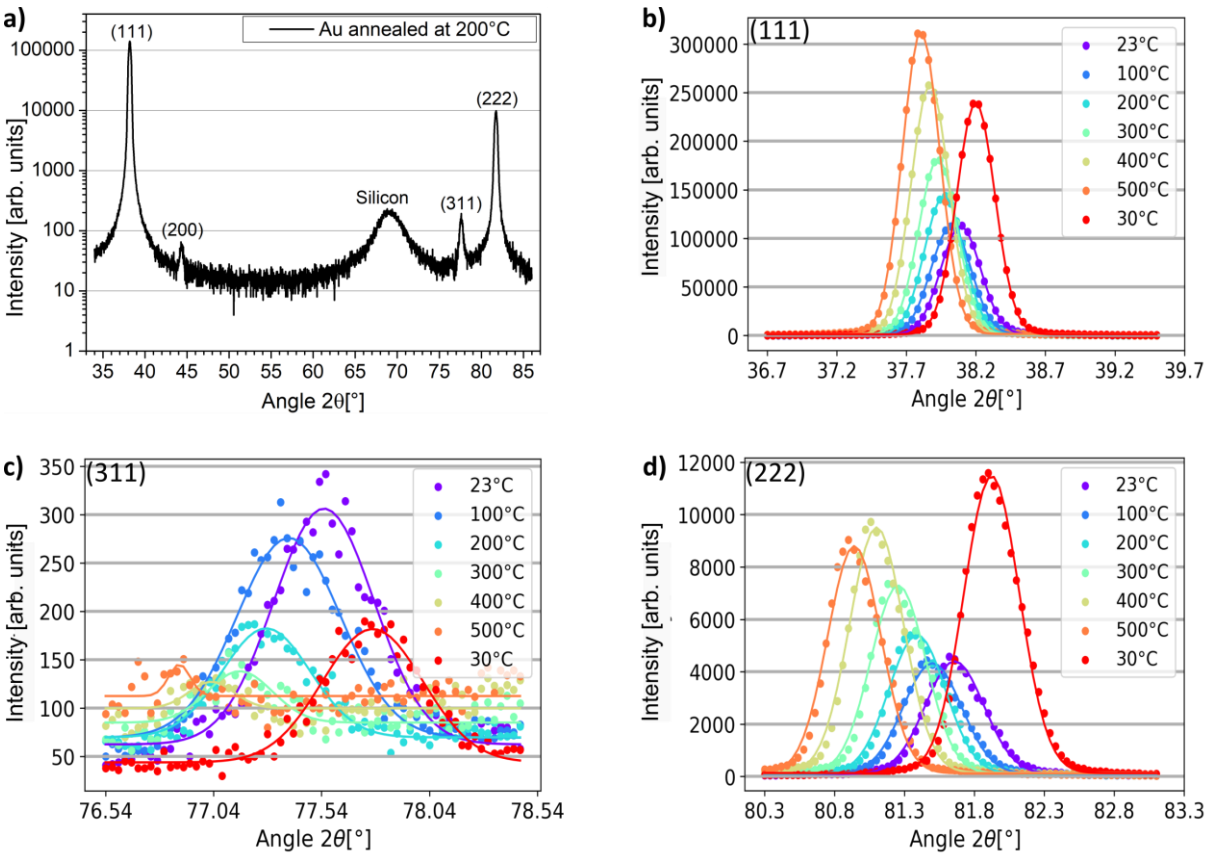

Fig. 6: a) XRD curve obtained on gold deposited at 0.2 nm/s and annealed at 200 °C for 20 min. b) to d) XRD curves of the (111), (311) and (222) gold orientations during annealing. The dots are the data, and the lines are the Gaussian fits.

The identification of the peaks is made with the gold and silicon crystallographic datasheets. The peaks at 38.18 °, 44.36 °, 77.62 ° and 81.74 ° respectively correspond to the (111), (200), (311) and (222) gold orientations. The peak marked as silicon corresponds to the (400) silicon substrate orientation. We tried to suppress this monocrystalline silicon peak by tilting the sample, but it remains with lower intensity. As X-Ray beam penetrates through the 200 nm gold layer, the XRD analysis is meaningful for both gold surfaces: gold before stripping (cf. Fig. 1B) and gold after stripping (cf. Fig. 1D). Without considering silicon, the peaks of the (111), (311) and (222) gold orientations are the most intense peaks kept for the rest of the study.

In the XRD graphs of the (111) and (222) gold orientations (cf. Fig. 6b and d), up to 400°C, the peak intensity increases, which means the number of atomic planes matching this

orientation increase. However, at 500°C, (111) peak intensity is still increasing while surprisingly (222) peak intensity decreases. Since the (111) and (222) planes correspond to the same crystallographic orientation, the slight differences in peak intensity variations (cf. Fig. 6) and crystallite size (Fig. 7) is assigned to the measurement time between the data acquisition of each peak.

In the case of (311) orientation (cf. Fig. 6c), the number of planes decreases with the rise in annealing temperature. The intensity of the curves at 400°C and 500°C decreases resulting in more prominent noise which increases the standard error on crystallite size. Once returned to ambient temperature, the intensity of (311) peak is sufficiently high to be detected without much noise but remains below the initial value.

It must be noted that the gold layer was dewetted at the end of the measurement. So, the results presented for the annealing at 500 °C and after cooling the sample are influenced by this dewetting. In the case of the (311) orientation at 500 °C, more nuance must be provided, due to dewetting, the obtained fit is surely not representative of the true gold state which explains why the (311) oriented crystallite size at 500 °C is as large as the gold layer with a standard deviation allowing even larger thicknesses than gold layer. AFM measurements proves that the dewetting begins before 10min of annealing, therefore the annealing at 500°C is discarded for the subsequent steps of the study. The dewetting AFM results and their discussion are presented in subsection 5.4.

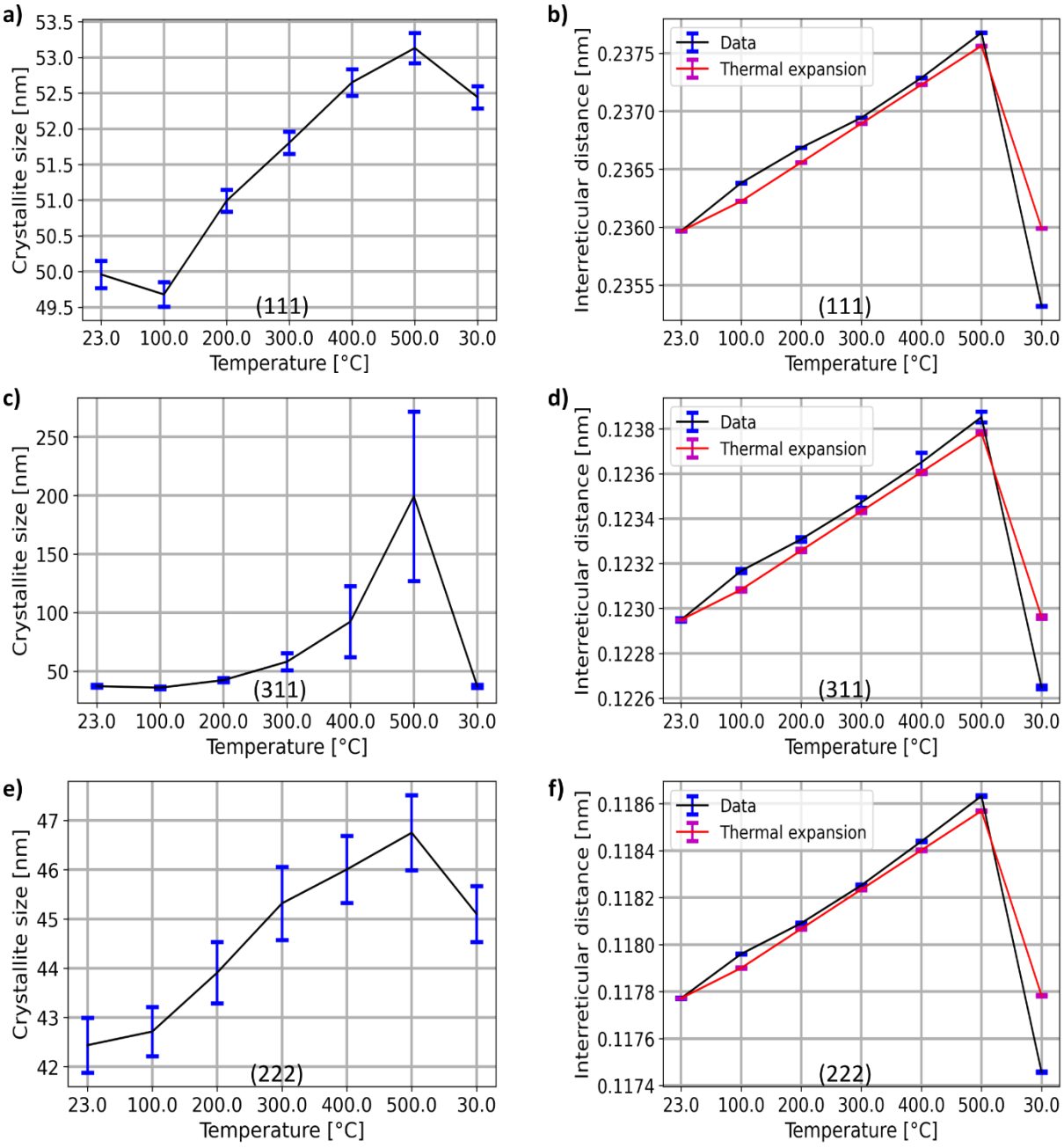

Fig. 7: a), c) and e) Crystallite size of the (111), (311) and (222) gold orientations respectively. b), d) and f) Comparison between the variation in interreticular distance due to temperature and the theoretical thermal expansion of the interreticular distance for the (111), (311) and (222) gold orientations respectively. The vertical blue bars are error bars.

The mean crystallite size (cf. Fig. 7a, c and e) is computed with Scherrer equation (eq. 3-1) using parameters derived from the Gaussian fits in Fig. 6. This size represents the crystallite width normal to the surface in symmetric mode. For all orientations, the size of the crystallites increases with the temperature. This result could sound strange as the (311) peak intensity decreases with temperature. But the crystallite size is affected by the thermal

expansion. Indeed, the (311) orientation keep the same size before and after annealing. The increase observed from 20 °C to 400 °C could only come from the thermal dilation. When the sample have been cooled after annealing the crystallite size of all the orientation decreased. This phenomenon is also due to the thermal expansion.

Finally, all the XRD graphs show peak shifting to lower angles (cf. Fig. 6b to d). This behavior is expected as the thermal dilation broaden the interreticular distances. However, once back to ambient temperature, the peak at 30 °C is not at the same position as the initial peak at 23°C, which might be attributed to residual stress in the gold layer. To confirm that the peak shifting is due to thermal dilation, the evolution of the interreticular distance versus the annealing temperature is plotted and compared to the expected evolution due to thermal dilatation (cf. Fig. 7b, d and f). For all the orientations, the effective evolution follows quite accurately the expected evolution. The differences observed at some points, mainly when back to ambient temperature, are symptomatic of the presence of stresses inside the crystallites. The vertical deformations ($\varepsilon^{\perp} = (d_{30°C} - d_{20°C})/d_{20°C}$ where d stands for the interreticular distance) induced by these stresses after annealing are -3x10^{-4} and -2x10^{-4} respectively for (111) and (311) orientations.

4.3. XRD measurements during isotherms

The temperatures selected for the isotherm study are 300 °C and 400 °C. Indeed, as shown previously, high temperatures induce predominant and large (111) oriented crystallite. We will justify more in details these temperatures in the subsection 5.2. In this part, we will examine the effect of each isotherm on each orientation.

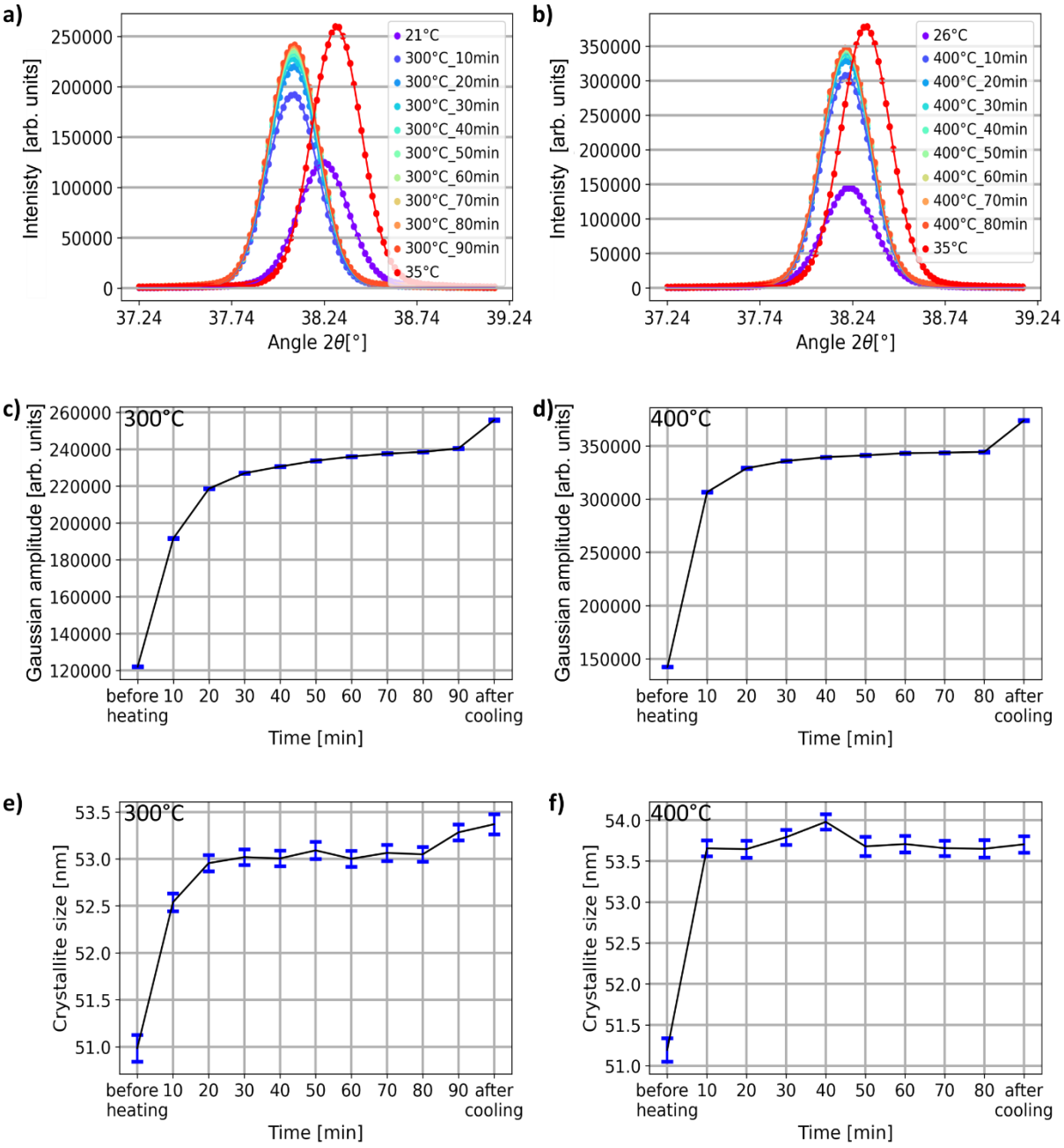

Fig. 8: a) and b) XRD curves of the (111) gold orientations during annealing at the 2 isotherms: 300 °C and 400 °C respectively. The dots are the data, and the lines are the Gaussian fits. The time specified in the caption are the annealing time. c) and d) Gaussian amplitude of the (111) gold orientation during annealing at 300 °C and 400 °C respectively, obtained from the Gaussian fits in a) and b). e) and f) Crystallite size of the (111) gold orientation during isothermal annealing at 300 °C and 400 °C respectively. The vertical blue bars are error bars.

As the Gaussian curves are fairly overlapping (cf. Fig. 8a and b), the Gaussian amplitudes of the (111) gold orientation have been plotted versus the annealing time (cf. Fig. 8 c and d). The blue error bars represent the standard error on the amplitude estimation. For the isotherms at 300 °C and 400°C, the Gaussian amplitude increases with the temperature and

the annealing time. For an annealing at 300 °C, the amplitude increases until the end of the measurement (90 min). The same behavior is observed at 400 °C but the amplitude stabilizes since 50 min. Once cooled, the (111) Bragg peak amplitude, and so the number of (111) planes, increases in the case of the annealing at 300 °C and 400 °C. From a crystallite size point of view (cf. Fig. 8 e and f), an annealing at 400 °C creates larger crystallites than at 300 °C. Moreover, the crystallite size remains constant at 300 °C up to 80 min and at 400 °C during the whole annealing since the first measurement at 10min. The crystallite size is considered constant on each interval as the error bars, standing for the standard error, are overlapping. At 90 min for 300 °C and 40 min for 400 °C, the crystallite size increases but, in the case of 400°C for 40min, the increase is not significant as error bars overlap. However, the cooling does not affect the final size here.

Finally, Fig. 9 introduces the effect of annealing on (311) orientation. As we want to maximize the presence of (111) grains, we need to decrease or suppress the other orientations. This purpose is achieved as the Gaussian intensity decreases as soon as the annealing reaches the right temperatures. The Fig. 9c) and d) allow a better insight on the Gaussian amplitudes as the curves during annealing are overlapping (cf. Fig. 9a and b) and the y-level of the Gaussian base significantly influences the peak height in Fig. 9a) and b). Once annealing begun at 300 °C and 400 °C, the Gaussian amplitude, and so the number of (311) planes, remains constant as the error bars are overlapping. Yet, the amplitude at 400 °C is lower than at 300 °C. Similarly, their size stays quite constant during annealing even if there is a slight increase at 300 °C for 50 min. For the annealing at 300 °C, the size before heating and after cooling is the same. So, the increasing size can be attributed to thermal expansion. But, at 400 °C, the size after cooling is a little higher than the initial size.

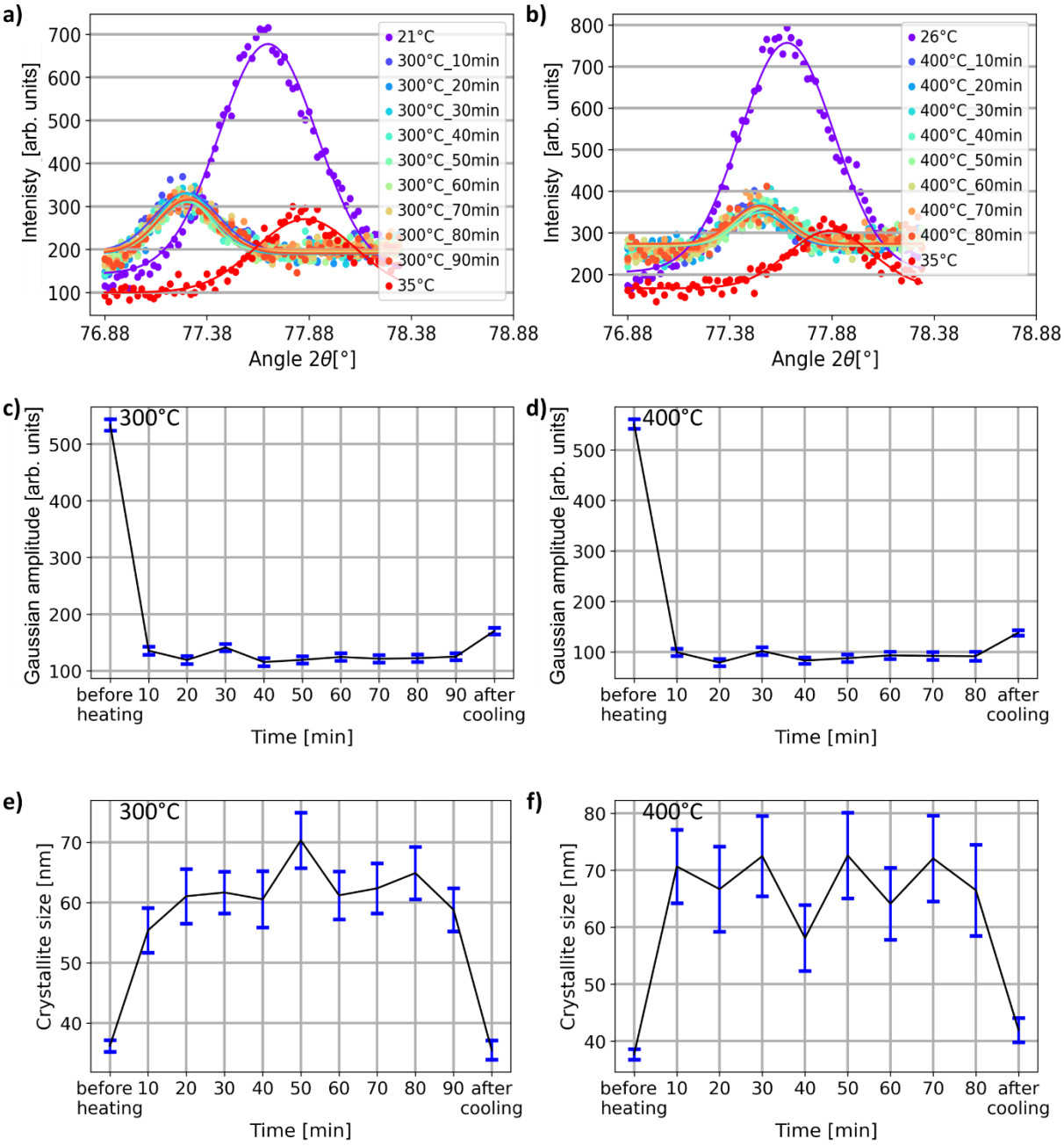

Fig. 9: a) and b) XRD curves of the (311) gold orientations during annealing at the 2 isotherms: 300 °C and 400 °C respectively. The dots are the data, and the lines are the Gaussian fits. The time specified in the caption are the annealing time. c) and d) Gaussian amplitude of the (311) gold orientation during annealing at 300 °C and 400 °C respectively, obtained from the Gaussian fits in a) and b). e) and f) Crystallite size of the (311) gold orientation during isothermal annealing at 300°C and 400 °C respectively. The vertical blue bars are error bars.

To summarize, we have determined the right deposition rate (0.2 nm/s) for gold in ambient condition. Moreover, we have determined two temperatures (300 °C and 400 °C) for which the deposited gold has the maximum and the largest (111) orientated crystallites. Now, we need to determine the annealing time which further maximizes the (111)

orientation and its crystallites. To this end, XRD is performed during isotherm respectively at 300 °C and 400 °C.

4.4. AFM measurements in resonant-mode on optimized temperature-annealing time couples

As it will be detailed in part 5.2, two couples of annealing temperature and time have been selected from XRD measurements: 300 °C during 90 min (cf. Fig. 10) and 400 °C during 40 min (cf. Fig. 11). The last screening is performed with AFM on AuTS samples (cf. Fig. 1D), annealed before stripping step.

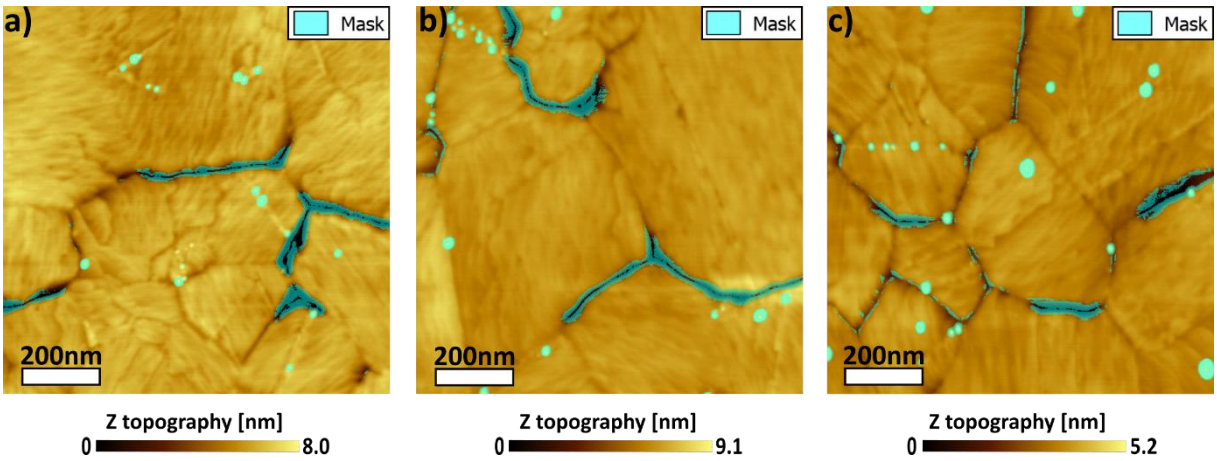

Fig. 10: AFM images on AuTS2As samples annealed at 300 °C during 90 min. a) to c) Different imaged areas. The blue mask represents area with strong height variations so that the non-masked surface exhibits a rms roughness less than or equal to 0.3 nm.

After annealing at 300 °C during 90 min, the surface exhibits a mean rms roughness of (0.5±0.1) nm with a useful surface of (97±1) %. As indicated in the caption of Fig. 10, the blue mask has been applied on the height variation so that the rms roughness of the surface is equal or inferior to 0.3 nm. This mask covers crystallite boundaries and adsorbates with large height variations on the gold surface which appear as blue spots on Fig. 10. The rms

roughness and useful surface do not take into account the adsorbates as they are not representative of the gold surface.

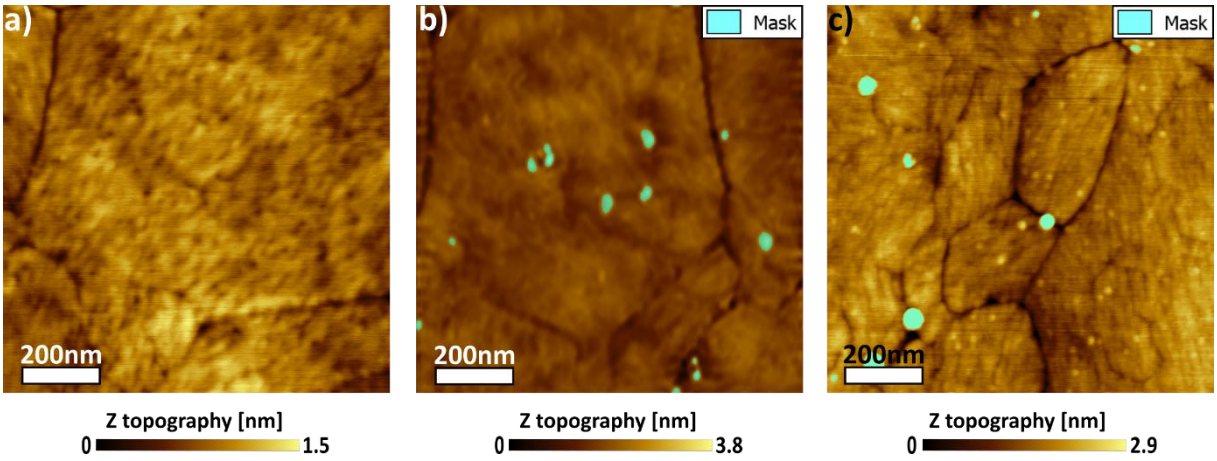

Fig. 11: AFM images on AuTS2As samples annealed at 400 °C during 40 min. a) to c) Different imaged areas. The blue mask represents adsorbates so that the non-masked surface exhibits a rms roughness inferior or equal to 0.3 nm.

Increasing the temperature to 400 °C and annealing for 40 min (cf. Fig. 11) smooth the surface up to (0.21±0.04) nm resulting in a useful surface close to 100 %. As the mask is only applied on adsorbates, neither the rms roughness nor the useful surface are taken into account.

5. Discussion

5.1. Choice of the deposition rate

In order to choose the deposition rate, two parameters are taken into account: the rms roughness and the useful surface (cf. Table 1), determined by AFM. The importance of roughness is based on its effect on molecule organization. An increasing roughness of the surface will promote molecular disorganization. As observed above, even if the roughness is higher than the 0.3 nm limit, some part of the surface could have a sufficiently low rms roughness. These surface parts composed the useful surface. The deposition rate giving the lowest rms roughness and the highest useful surface are chosen.

The deposition rate at 0.2 nm/s gives the lowest rms roughness, the higher useful surface and the lowest interval error for each parameter.

Table 1: Comparison of the different depositions rates with all sample annealed at 200 °C during 20 min

	AuTS0.5As	AuTS2As	AuTS50As
RMS Roughness [nm]	(1.0±0.7)	(0.26±0.03)	(0.9±0.2)
Useful surface [%]	(95±3)	100	(79±18)

5.2. XRD result analysis: selection of temperature and annealing time couple

As observed in Fig. 7, the higher the temperature, the higher the (111) and (222) oriented crystallites size and number. Besides, the (311) Bragg peak amplitude decreases with the temperature and their size remains the same before and after annealing. Two different temperatures are investigated for isotherm study: 300 °C and 400 °C.

At 300°C, the number of (111) planes (cf. Fig. 8a, c and e) increases until the end of the experiments. The crystallite size is the same for 80 min and then rise at 90 min. Moreover, the (311) orientation (cf. Fig. 9a, c and e) is not really influenced by annealing time. Thus, it appears that annealing for 90 min at 300 °C gives the most (111) and largest crystallites.

For the isotherm at 400 °C, a similar behavior is observed for (111) (cf. Fig. 8b, d and f) and (311) crystallites (cf. Fig. 9b, d and f) but some differences appear. After 60 min, the number of (111) planes is constant whereas the (311) crystallites undergo a slight decrease of their size at 40 min but the error bar at 40 min overlaps the ones at 20 min, 60 min and 80 min. Thus, this slight decrease is not significant. As annealing at 400 °C for 40 min is a little

more noteworthy than the other annealing times for this temperature, this temperature-annealing time couple is selected.

5.3. Determining the optimal temperature and annealing time

From the latter section, 2 couples of temperature and annealing time have been determined optimal. The last screening is based on AFM analysis on AuTS (cf Fig. 1D): the couple which leads to the lowest rms roughness and the highest useful surface is selected.

Table 2: Surface states summary of gold annealed with the different temperature-annealing time couples.

	200 °C for 20 min	300 °C for 90 min	400 °C for 40 min
RMS Roughness [nm]	(0.26±0.03)	(0.5±0.1)	(0.21±0.04)
Useful surface [%]	100	(97±1)	100

The sample surface annealed at 400 °C for 40 min is smoother than the one annealed at 300 °C for 90 min (cf. Table 2). Therefore, the annealing at 400 °C for 40 min is the optimal couple.

However, during the deposition rate selection phase (cf. part 4.1), the sample AuTS2As, arbitrary annealed at 200 °C during 20 °C, gave a rms roughness and an useful surface comparable to the one annealed at 400 °C for 40 min (cf. Table 2). But, the Gaussian amplitude of Au(111) orientation peak, after an annealing at 200 °C during 20 min (cf. Fig. 6a), is two times lower than the Gaussian amplitude of Au(111) orientation peak after an annealing at 400 °C for 40 min (cf. Fig. 8d). Besides, the (111) crystallites are bigger at 400 °C during 40 min (53.98 nm) than at 200 °C for 20 min (51.24 nm). Therefore, the optimal temperature and annealing time for gold evaporated on silicon in ambient conditions is 400 °C for 40 min.

In order to compare the results obtained for the optimal deposition rate and annealing with the literature[13,15,16], we have performed AFM measurement recording 5x5 µm² images of our optimized AuTS. These measures reveal again an ultra-flat surface, suitable for nanoscience fields like molecular electronics, with a RMS roughness of (0.25±0.03) nm and a useful surface of 100 % (cf. Fig. 12). The suitability for SAM deposition is discussed in the subsection 5.5.

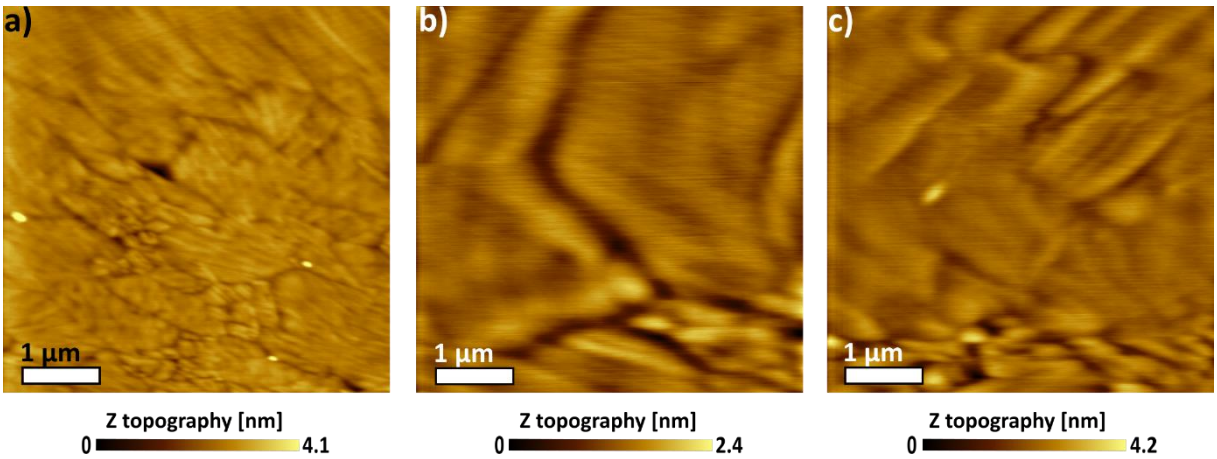

Fig. 12: AFM images on AuTS2As samples annealed at 400 °C during 40 min. a) to c) Different imaged areas.

5.4. Dewetting effects on AuTS roughness

AFM measurements are performed to prove that the dewetting begins before 10min of annealing at 500 °C.

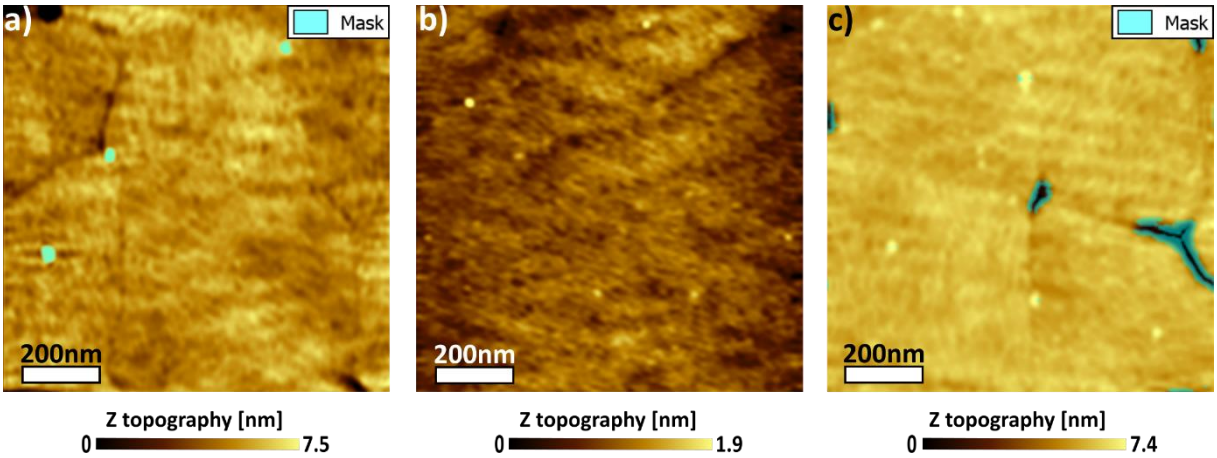

Fig. 13: AFM images on AuTS2As samples annealed at 500 °C for 10 min. a) to c) Different imaged areas. The blue mask represents area with height variations so that the non-masked surface exhibits a rms roughness inferior or equal to 0.3 nm.

At 500 °C during 10 min (cf. Fig. 13), the mean rms roughness increases to (0.3±0.1) nm. The useful surface is about 100 %. For Fig. 13a), the mask is only applied on adsorbates. Nevertheless, the interval error of the annealing at 500 °C overlaps the one at 400 °C. So, the increase in roughness is not certain. However, the standard error at 500 °C is 3 times greater than the one at 400 °C.

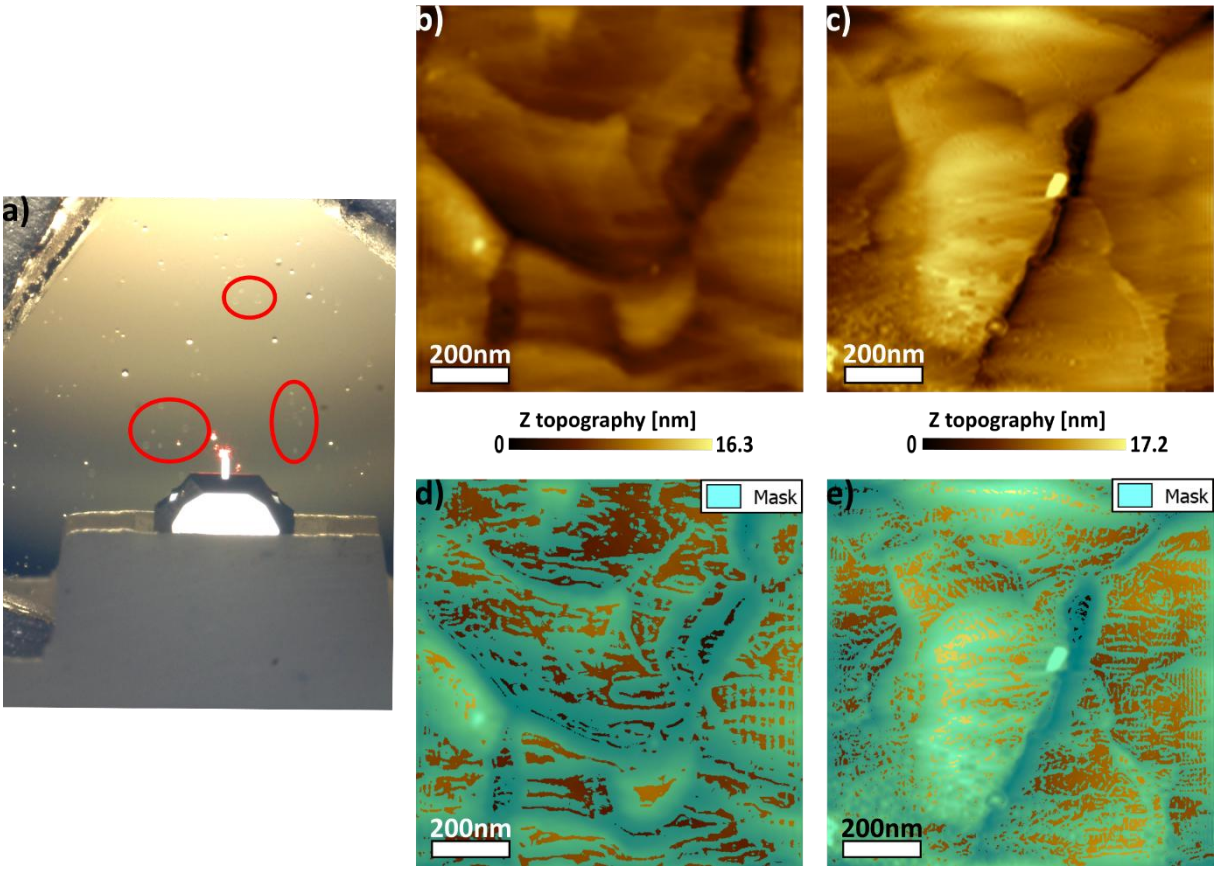

Fig. 14: AFM images on AuTS2As samples annealed at 500 °C for 10 min made on the shaded areas. a) Photo of the gold surface with the AFM tip. The red circles highlight the shaded areas on gold. b) and c) Topographic images on different shaded areas. d) and e) Application of the mask to reveal the useful surface on b) and c) respectively. The blue mask represents area with strong height variations so that the non-masked surface has a rms roughness inferior or equal to 0.3 nm

Moreover, the surface of the sample annealed at 500 °C during 10 min exhibits zones with colors slightly different from the rest of the gold surface (cf. Fig. 14). These shaded zones reveal a gold with high rms roughness (2.1±0.6) nm, (cf. Fig. 14b and c) and a low useful surface (24±1) %. As explained in the part 4.3, the annealing at 500 °C has encountered dewetting. The presence of these shaded areas with high roughness tends to prove the presence of partial dewetting at multiple locations on the gold surface even with 10 min of annealing.

5.5. Suitability for SAM deposition

The presence of large atomically flat terraces is a parameter that indicates the suitability of the surface with a low roughness for molecule deposition. This has been probed by

acquiring STM images at ambient conditions in air on AuTS deposited at 0.2 nm/s and annealed at 400°C during 40 min (cf. Fig. 15).

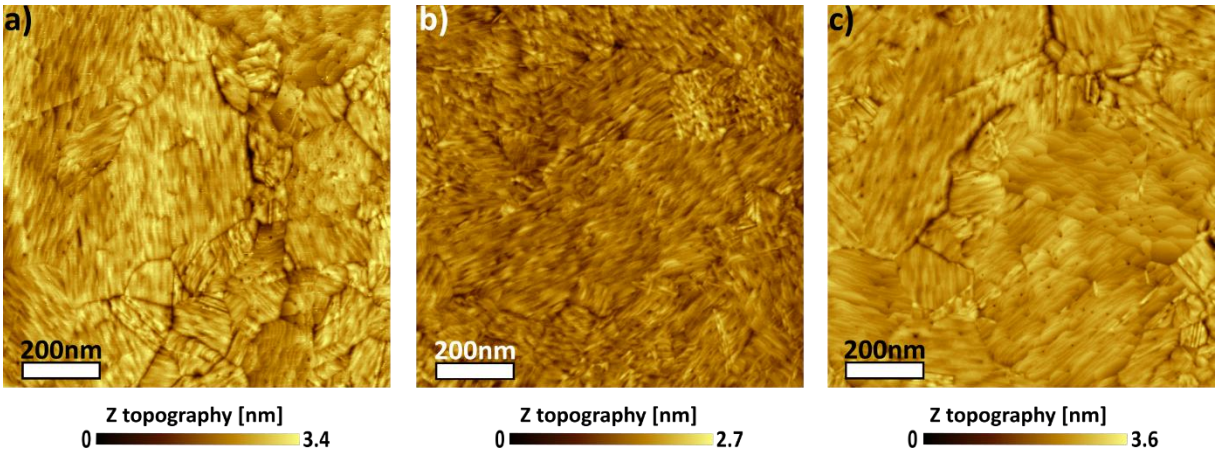

Fig. 15: STM images on AuTS2As samples annealed at 400 °C during 40 min. a) to c) Different imaged areas. The largest terraces are observed in the top right corner on a) and in the middle right of c).

As displayed in Fig. 15, the largest terraces (up to ~100 nm) are observed in a), top right corner, and c), middle right, ,and they are smaller than those of Diebel's images[12]. The rest of the grains are also terraces but stacked in a way they practically overlap each other. Therefore, if atomically flat terraces are present on our AuTS, there are no large ones. Nevertheless, electrochemical analysis with CV is performed to verify how molecules organize on our AuTS.

Cyclic voltammogram obtained on bare AuTS substrate is shown in Fig. 16. This experiment is important to perform prior to SAM characterization to calculate the real surface of the electrode. The voltammogram observed is very clean with well-defined baseline. The real surface area is calculated by integrating the oxygen reduction peak (around 0.82 V) by following Trasatti's method [44]. From Fig. 16, the real active surface area calculated is 0.56 cm^2 and comparing with geometrical surface area: $S_{real}/S_{geometrical}$ = 0.56/0.5 = 1.12. Hence, the AuTS substrate is really flat at atomic scale and suitable for SAM deposition.

To verify the above statement on flatness of AuTS substrate, CV is performed SAM of $FcC_{11}SH$ deposited on optimized AuTS. An ethanolic solution of 1 mM $FcC_{11}SH$ is prepared and degassed with nitrogen for 10 minutes. A freshly template stripped AuTS substrate is soaked in this solution and the solution is degassed again for 10 minutes. Then the solution with AuTS substrate is left for 20 hours at room temperature under nitrogen (using balloon filled with N_2). After 20 hours, the AuTS substrate is taken out and washed with copious amount of ethanol. The substrate is dried by blowing nitrogen and CV is performed. Fig. 17 shows the voltammogram taken at 1 V/s.

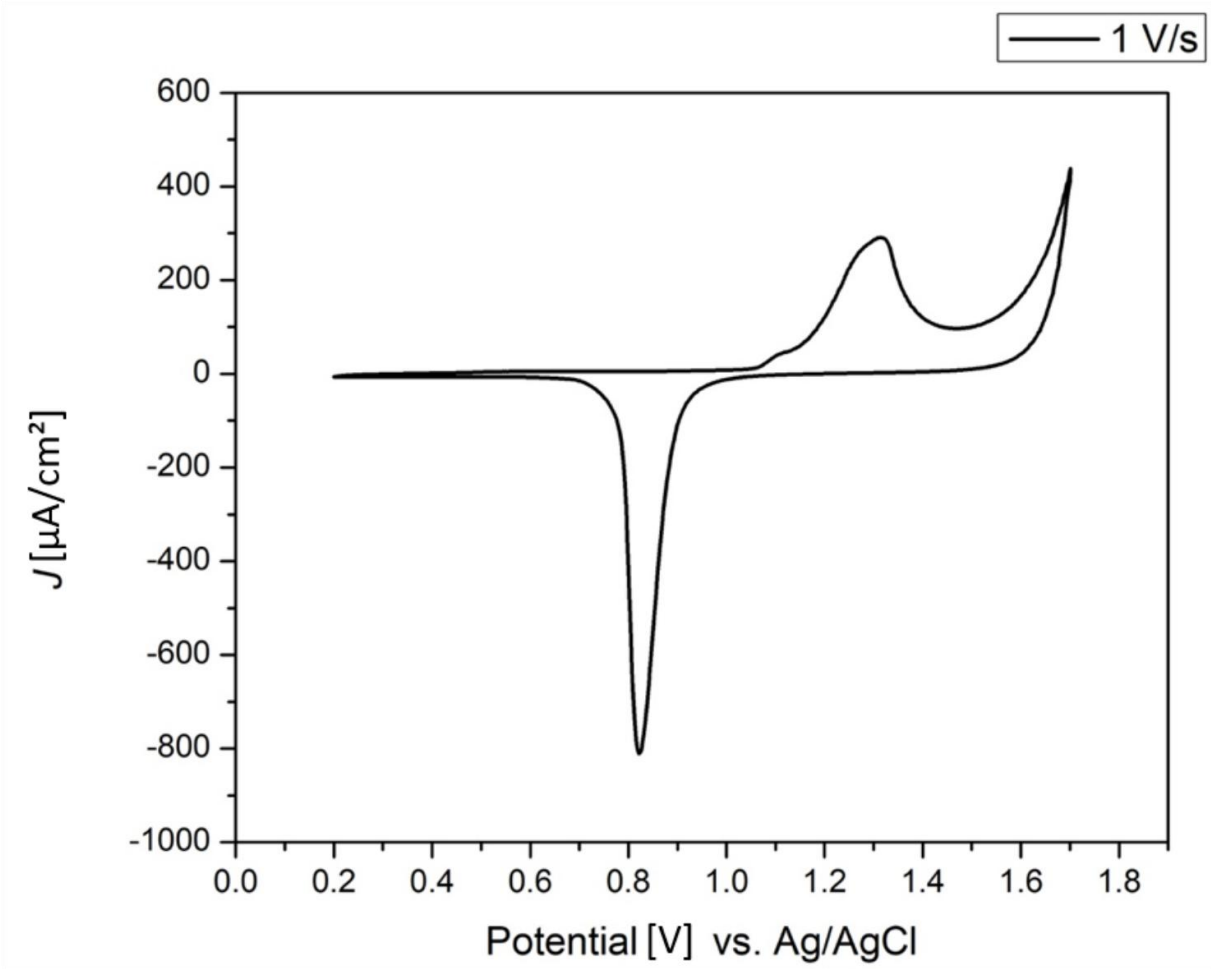

Fig. 16: Cyclic voltammogram of bare AuTS2As, annealed at 400 °C during 40 min, recorded at scan rate of 1 V/s with Ag/AgCl reference electrode and 1 M $HClO_4$ electrolyte solution.

The Fig. 17 voltammogram has a peak-separation of 0.075 V indicating fast electron transfer. FWHM of the redox peaks is 80 mV. Integrating the redox peaks and applying the following formula $\Gamma_{Fc} = Q_{tot}/nFA$ (Q_{tot}: total charge, n: number of electrons transferred per mole of reaction, F: Faraday constant and A: real surface area of the electrode exposed to electrolyte solution), molecular density Γ_{Fc} is 4.3×10^{-10} mol/cm^2. Compare to the maximal theoretical value (4.5×10^{-10} mol/cm²), the computed molecular density is very close to the maximum density. All the above quantifications indicate near ideal behavior of the voltammogram and densely packed SAM [30,45].

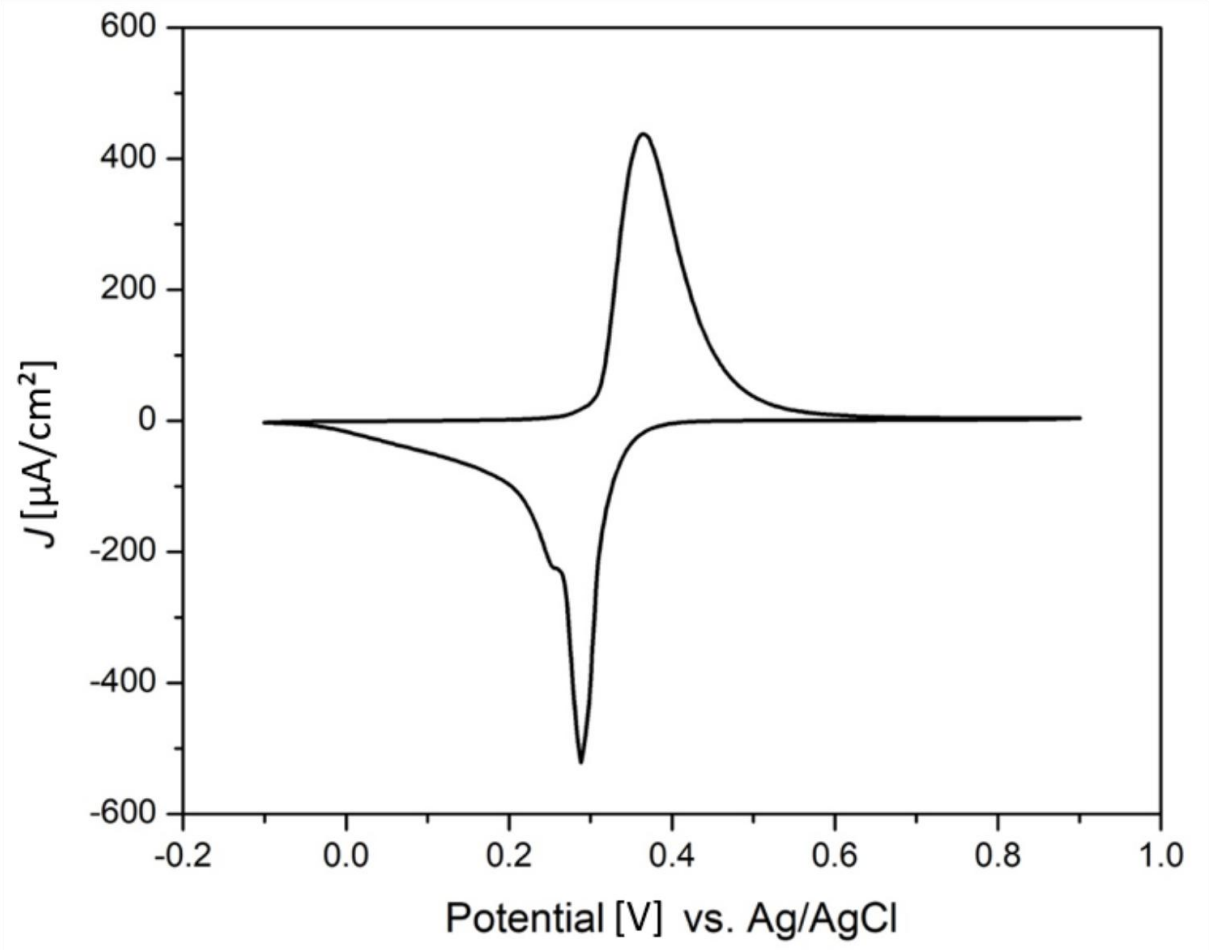

Fig. 17: Cyclic voltammogram of AuTS2As, annealed at 400 °C during 40 min, modified with a of $FcC_{11}SH$ recorded at scan rate of 1V/s with Ag/AgCl reference electrode and 1 M $HClO_4$ electrolyte solution.

6. Conclusion

In summary, we have determined the optimal deposition rate (0.2 nm/s) and annealing temperature (400°C) and time (40 min) of gold deposited on silicon, with the annealing performed in ambient conditions after deposition. The purposes are to get an AuTS surface with minimum roughness and the largest (111) crystallites. Two techniques have been mainly used: AFM and XRD. AFM, in tapping and peak force mode, was used to determine the roughness of the AuTS surfaces, while in situ XRD during annealing, was employed to survey the crystalline orientation evolution with annealing. With the optimized parameters, AuTS surface exhibits a rms roughness of (0.21±0.04) nm with a (111) crystallite size of 54 nm normal to the surface. Such smooth surface makes them suitable for nanoscience fields like molecular electronics.

Acknowledgment

We thank Mr. Olivier Hector of the Fresnel Institute for the gold depositions used in this study.

Funding sources

This research receives grant from Aix-Marseille University doctoral school.

References

[1] J.P. Hirth, G.M. Pound, Evaporation of Metal Crystals, J. Chem. Phys. 26 (1957) 1216–1224. https://doi.org/10.1063/1.1743496.

[2] G. Thurner, R. Abermann, Internal stress and structure of ultrahigh vacuum evaporated chromium and iron films and their dependence on substrate temperature and oxygen partial pressure during deposition, Thin Solid Films. 192 (1990) 277–285. https://doi.org/10.1016/0040-6090(90)90072-L.

[3] J. Safarian, T.A. Engh, Vacuum Evaporation of Pure Metals, Metall. Mater. Trans. A. 44 (2013) 747–753. https://doi.org/10.1007/s11661-012-1464-2.

[4] L. Jiang, T. Wang, C.A. Nijhuis, Fabrication of ultra-flat silver surfaces with sub-micrometer scale grains, Thin Solid Films. 593 (2015) 26–39. https://doi.org/10.1016/j.tsf.2015.09.023.
[5] C. Chia, S.S. Jeffrey, R.T. Howe, Scalable methods for ultra-smooth platinum in nanoscale devices, Micro Nano Eng. 3 (2019) 50–58. https://doi.org/10.1016/j.mne.2019.04.002.
[6] P. Mogyorósi, T. Szörényi, K. Bali, Zs. Tóth, I. Hevesi, Pulsed laser ablative deposition of thin metal films, Appl. Surf. Sci. 36 (1989) 157–163. https://doi.org/10.1016/0169-4332(89)90909-4.
[7] O. Sneh, R.B. Clark-Phelps, A.R. Londergan, J. Winkler, T.E. Seidel, Thin film atomic layer deposition equipment for semiconductor processing, Thin Solid Films. 402 (2002) 248–261. https://doi.org/10.1016/S0040-6090(01)01678-9.
[8] R.G. Parkhomenko, N.B. Morozova, G.I. Zharkova, Y.V. Shubin, S.V. Trubin, V.V. Kriventsov, B.M. Kuchumov, T.P. Koretskaya, I.K. Igumenov, Deposition of Au Thin Films and Nanoparticles by MOCVD, Chem. Vap. Depos. 18 (2012) 336–342. https://doi.org/10.1002/cvde.201207004.
[9] M. Emami, R. Goodarzi, Optoelectronic correlations for gold thin films in different annealing temperature, Optik. 171 (2018) 397–403. https://doi.org/10.1016/j.ijleo.2018.06.075.
[10] D. Gu, C. Zhang, Y.-K. Wu, L.J. Guo, Ultrasmooth and Thermally Stable Silver-Based Thin Films with Subnanometer Roughness by Aluminum Doping, ACS Nano. 8 (2014) 10343–10351. https://doi.org/10.1021/nn503577c.
[11] P.N. Nirmalraj, H. Schmid, B. Gotsmann, H. Riel, Nanoscale Origin of Defects at Metal/Molecule Engineered Interfaces, Langmuir. 29 (2013) 1340–1345. https://doi.org/10.1021/la3046109.
[12] J. Diebel, H. Löwe, P. Samorí, J.P. Rabe, Fabrication of large-scale ultra-smooth metal surfaces by a replica technique, Appl. Phys. Mater. Sci. Process. 73 (2001) 273–279. https://doi.org/10.1007/s003390100935.
[13] E.A. Weiss, G.K. Kaufman, J.K. Kriebel, Z. Li, R. Schalek, G.M. Whitesides, Si/SiO_2-Templated Formation of Ultraflat Metal Surfaces on Glass, Polymer, and Solder Supports: Their Use as Substrates for Self-Assembled Monolayers, Langmuir. 23 (2007) 9686–9694. https://doi.org/10.1021/la701919r.
[14] C. Masens, J. Schulte, M. Phillips, S. Dligatch, Ultra Flat Gold Surfaces for Use in Chemical Force Microscopy: Scanning Probe Microscopy Studies of the Effect of Preparation Regime on Surface Morphology, Microsc. Microanal. 6 (2000) 113–120. https://doi.org/10.1007/s100059910010.
[15] M. Hegner, P. Wagner, G. Semenza, Ultralarge atomically flat template-stripped Au surfaces for scanning probe microscopy, Surf. Sci. 291 (1993) 39–46. https://doi.org/10.1016/0039-6028(93)91474-4.
[16] P. Wagner, M. Hegner, H.-J. Guentherodt, G. Semenza, Formation and in Situ Modification of Monolayers Chemisorbed on Ultraflat Template-Stripped Gold Surfaces, Langmuir. 11 (1995) 3867–3875. https://doi.org/10.1021/la00010a043.
[17] M.H. Dishner, M.M. Ivey, S. Gorer, J.C. Hemminger, F.J. Feher, Preparation of gold thin films by epitaxial growth on mica and the effect of flame annealing, J. Vac. Sci. Technol. Vac. Surf. Films. 16 (1998) 3295–3300. https://doi.org/10.1116/1.581536.

[18] L.T. Banner, A. Richter, E. Pinkhassik, Pinhole-free large-grained atomically smooth Au(111) substrates prepared by flame-annealed template stripping, Surf. Interface Anal. 41 (2009) 49–55. https://doi.org/10.1002/sia.2977.
[19] S. Borukhin, B. Pokroy, Formation and Elimination of Surface Nanodefects on Ultraflat Metal Surfaces Produced by Template Stripping, Langmuir. 27 (2011) 13415–13419. https://doi.org/10.1021/la203596p.
[20] R. Ragan, D. Ohlberg, J.J. Blackstock, S. Kim, R.S. Williams, Atomic Surface Structure of UHV-Prepared Template-Stripped Platinum and Single-Crystal Platinum(111), J. Phys. Chem. B. 108 (2004) 20187–20192. https://doi.org/10.1021/jp0466789.
[21] J.M. Tour, L. Jones, D.L. Pearson, J.J.S. Lamba, T.P. Burgin, G.M. Whitesides, D.L. Allara, A.N. Parikh, S. Atre, Self-Assembled Monolayers and Multilayers of Conjugated Thiols, .alpha.,.omega.-Dithiols, and Thioacetyl-Containing Adsorbates. Understanding Attachments between Potential Molecular Wires and Gold Surfaces, J. Am. Chem. Soc. 117 (1995) 9529–9534. https://doi.org/10.1021/ja00142a021.
[22] C.D. Bain, E.B. Troughton, Y.T. Tao, J. Evall, G.M. Whitesides, R.G. Nuzzo, Formation of monolayer films by the spontaneous assembly of organic thiols from solution onto gold, J. Am. Chem. Soc. 111 (1989) 321–335. https://doi.org/10.1021/ja00183a049.
[23] M.D. Porter, T.B. Bright, D.L. Allara, C.E.D. Chidsey, Spontaneously organized molecular assemblies. 4. Structural characterization of n-alkyl thiol monolayers on gold by optical ellipsometry, infrared spectroscopy, and electrochemistry, J. Am. Chem. Soc. 109 (1987) 3559–3568. https://doi.org/10.1021/ja00246a011.
[24] C.A. Reynaud, D. Duché, J. Le Rouzo, A. Nasser, L. Nony, F. Pourcin, O. Margeat, J. Ackermann, G. Berginc, C.A. Nijhuis, L. Escoubas, J.-J. Simon, Enhancing Reproducibility and Nonlocal Effects in Film-Coupled Nanoantennas, Adv. Opt. Mater. 6 (2018) 1801177. https://doi.org/10.1002/adom.201801177.
[25] V. Jangid, D. Brunel, C. Lebouin, C.A. Reynaud, E. Sanchez-Adaime, D. Duche, F. Dumur, J.-J. Simon, G. Berginc, C.A. Nijhuis, L. Escoubas, Self-Assembly and Electrochemical Characterization of Ferrocene-based Molecular Diodes for Solar Rectenna Device, MRS Adv. 5 (2020) 3185–3194. https://doi.org/10.1557/adv.2020.401.
[26] Y. Feng, E.R. Dionne, V. Toader, G. Beaudoin, A. Badia, Odd–Even Effects in Electroactive Self-Assembled Monolayers Investigated by Electrochemical Surface Plasmon Resonance and Impedance Spectroscopy, J. Phys. Chem. C. 121 (2017) 24626–24640. https://doi.org/10.1021/acs.jpcc.7b08053.
[27] L.P. Méndez De Leo, E. de la Llave, D. Scherlis, F.J. Williams, Molecular and electronic structure of electroactive self-assembled monolayers, J. Chem. Phys. 138 (2013) 114707. https://doi.org/10.1063/1.4795575.
[28] X.D. Cui, X. Zarate, J. Tomfohr, O.F. Sankey, A. Primak, A.L. Moore, T.A. Moore, D. Gust, G. Harris, S.M. Lindsay, Making electrical contacts to molecular monolayers, Nanotechnology. 13 (2002) 5–14. https://doi.org/10.1088/0957-4484/13/1/302.
[29] L. Yuan, L. Jiang, B. Zhang, C.A. Nijhuis, Dependency of the Tunneling Decay Coefficient in Molecular Tunneling Junctions on the Topography of the Bottom Electrodes, Angew. Chem. 126 (2014) 3445–3449. https://doi.org/10.1002/ange.201309506.
[30] C.A. Nijhuis, W.F. Reus, G.M. Whitesides, Mechanism of Rectification in Tunneling Junctions Based on Molecules with Asymmetric Potential Drops, J. Am. Chem. Soc. 132 (2010) 18386–18401. https://doi.org/10.1021/ja108311j.
[31] L. Jiang, L. Yuan, L. Cao, C.A. Nijhuis, Controlling Leakage Currents: The Role of the Binding Group and Purity of the Precursors for Self-Assembled Monolayers in the

Performance of Molecular Diodes, J. Am. Chem. Soc. 136 (2014) 1982–1991. https://doi.org/10.1021/ja411116n.
[32] J. Chen, Z. Wang, S. Oyola-Reynoso, M.M. Thuo, Properties of Self-Assembled Monolayers Revealed via Inverse Tensiometry, Langmuir. 33 (2017) 13451–13467. https://doi.org/10.1021/acs.langmuir.7b01937.
[33] D. Stamou, D. Gourdon, M. Liley, N.A. Burnham, A. Kulik, H. Vogel, C. Duschl, Uniformly Flat Gold Surfaces: Imaging the Domain Structure of Organic Monolayers Using Scanning Force Microscopy, Langmuir. 13 (1997) 4. https://doi.org/10.1021/la962123w.
[34] N. Camillone, C.E.D. Chidsey, G. Liu, G. Scoles, Substrate dependence of the surface structure and chain packing of docosyl mercaptan self-assembled on the (111), (110), and (100) faces of single crystal gold, J. Chem. Phys. 98 (1993) 4234–4245. https://doi.org/10.1063/1.465030.
[35] H. Sellers, A. Ulman, Y. Shnidman, J.E. Eilers, Structure and binding of alkanethiolates on gold and silver surfaces: implications for self-assembled monolayers, J. Am. Chem. Soc. 115 (1993) 9389–9401. https://doi.org/10.1021/ja00074a004.
[36] C.E.D. Chidsey, D.N. Loiacono, T. Sleator, S. Nakahara, STM study of the surface morphology of gold on mica, Surf. Sci. 200 (1988) 45–66. https://doi.org/10.1016/0039-6028(88)90432-3.
[37] C. Worsch, M. Kracker, W. Wisniewski, C. Rüssel, Optical properties of self assembled oriented island evolution of ultra-thin gold layers, Thin Solid Films. 520 (2012) 4941–4946. https://doi.org/10.1016/j.tsf.2012.03.016.
[38] F. Ruffino, M.G. Grimaldi, Atomic force microscopy study of the growth mechanisms of nanostructured sputtered Au film on Si(111): Evolution with film thickness and annealing time, J. Appl. Phys. 107 (2010) 104321. https://doi.org/10.1063/1.3428467.
[39] G. Le Lay, The Au/Si(111) interface: Growth mode, energetics, structural and electronic properties, J. Cryst. Growth. 54 (1981) 551–557. https://doi.org/10.1016/0022-0248(81)90512-1.
[40] R.P. Anantatmula, A.A. Johnson, S.P. Gupta, R.J. Horylev, The gold-silicon phase diagram, J. Electron. Mater. 4 (1975) 445–463. https://doi.org/10.1007/BF02666229.
[41] U. Holzwarth, N. Gibson, The Scherrer equation versus the “Debye-Scherrer equation,” Nat. Nanotechnol. 6 (2011) 534–534. https://doi.org/10.1038/nnano.2011.145.
[42] D. Nečas, P. Klapetek, Gwyddion: an open-source software for SPM data analysis, Open Phys. 10 (2012). https://doi.org/10.2478/s11534-011-0096-2.
[43] P. Klapetek, D. Nečas, C. Anderson, Gwyddion user guide, (n.d.) 177.
[44] S. Trasatti, O.A. Petrii, Real surface area measurements in electrochemistry, Pure Appl. Chem. 63 (1991) 711–734. https://doi.org/10.1351/pac199163050711.
[45] F.-R.F. Fan, J. Yang, L. Cai, D.W. Price, S.M. Dirk, D.V. Kosynkin, Y. Yao, A.M. Rawlett, J.M. Tour, A.J. Bard, Charge Transport through Self-Assembled Monolayers of Compounds of Interest in Molecular Electronics, J. Am. Chem. Soc. 124 (2002) 5550–5560. https://doi.org/10.1021/ja017706t.

List of equation, figure and table captions